Quantification of multiple mixed contrast and tissue compositions using photon-counting spectral computed tomography

Tyler E. Curtis and Ryan K. Roeder*
University of Notre Dame, Department of Aerospace and Mechanical Engineering, Bioengineering Graduate Program, Notre Dame, Indiana, United States

Abstract. Quantitative material decomposition of multiple mixed, or spatially coincident, contrast agent (gadolinium and iodine) and tissue (calcium and water) compositions is demonstrated using photon-counting spectral computed tomography (CT). Material decomposition is performed using constrained maximum likelihood estimation (MLE) in the image domain. MLE is calibrated by multiple linear regression of all pure material compositions, which exhibits a strong correlation ($R^2 > 0.91$) between the measured x-ray attenuation in each photon energy bin and known concentrations in the calibration phantom. Material decomposition of mixed compositions in the sample phantom provides color material concentration maps that clearly identify and differentiate each material. The measured area under the receiver operating characteristic curve is >0.95, indicating highly accurate material identification. Material decomposition also provides accurate quantitative estimates of material concentrations in mixed compositions with a root-mean-squared error <12% of the maximum concentration for each material. Thus, photon-counting spectral CT enables quantitative molecular imaging of multiple spatially coincident contrast agent (gadolinium and iodine) and tissue (calcium and water) compositions, which is not possible with current clinical molecular imaging modalities, such as nuclear imaging and magnetic resonance imaging. [DOI: 10.1117/1.JMI.6.1.013501]

Keywords: contrast media; molecular imaging; quantitative material decomposition; photon-counting spectral computed tomography; tissue decomposition.

Paper 18184RR received Aug. 27, 2018; accepted for publication Jan. 22, 2019; published online Feb. 11, 2019.

1 Introduction

X-ray computed tomography (CT) provides three-dimensional anatomic imaging at high spatial and temporal resolution.[1–3] However, the identification of multiple contrast agent and tissue compositions, or molecular imaging, in CT is inhibited by similarity in the overall x-ray attenuation across the polychromatic x-ray photon energy spectrum. Thus, CT is primarily used to diagnose changes in anatomic morphology. Morphological anomalies can be indicative of disease states, but a definitive diagnosis often requires quantitative imaging or a level of soft tissue discrimination that is not possible with conventional CT.[4] In these cases, an adjunct imaging modality, such as positron-emission tomography (PET) or magnetic resonance imaging (MRI), is required to confirm an initial diagnosis. PET provides sensitive molecular imaging by tracking positron-emitting radionuclide imaging probes but requires simultaneous CT for anatomic imaging.[4–6] MRI provides enhanced soft tissue contrast but at a cost of extended time for image acquisition.[4] Thus, quantitative material identification using x-ray CT would benefit patients by reducing imaging time, cost, and radiation exposure.

Photon energy discrimination in x-ray CT, or multienergy CT, was first proposed as a method for material identification in 1970s.[7] Dual-energy CT (DECT) systems, which typically utilize two-photon energy source spectra via different tube potentials with an energy integrating detector, were subsequently developed in 1980s. DECT has enabled improved separation of two material components, e.g., bone or contrast agents versus soft tissue,[8,9] and three materials can be decomposed by applying a physical constraint, such a mass or volume conservation.[8,10,11] More recently, photon-counting detectors have enabled binning of photon energy spectra from a polychromatic source.[12–14] Photon-counting detectors were first used for measurements of high-energy, low flux spectra, but recent advances in detector materials and application-specific integrating circuits have enabled separation of high flux energy spectra and thus applications in photon-counting spectral CT.[14]

Prototype photon-counting spectral CT systems acquire multiple energy bins and, when used in conjunction with material decomposition algorithms, have been used to identify[15–17] and quantify[18–25] multiple discrete contrast agent and tissue compositions (Table 1). Quantitative material decomposition of binary mixtures of contrast agents in water (or three total materials, Table 1) has been demonstrated and validated by the mean absolute error versus known concentrations.[15,21,24,25] Moreover, these recent studies also demonstrated the ability of spectral CT to track multiple contrast agents longitudinally *in vivo*,[24,25] but analyses were limited to contrast agents, ignoring physiological fluids and tissues, and were not quantitatively validated. Thus, quantitative material decomposition of more than three spatially coincident contrast agent and tissue compositions has not been quantitatively validated (Table 1). Importantly, the quantification of multiple spatially coincident components in mixed compositions is not possible with current clinical molecular imaging modalities, such as PET and MRI, and thus offers the greatest

*Address all correspondence to Ryan K. Roeder, E-mail: rroeder@nd.edu

2329-4302/2019/$25.00 © 2019 SPIE

Table 1 Summary of previous experimental studies investigating quantitative material decomposition of multiple (more than two) contrast agent and tissue compositions by photon-counting spectral CT, highlighting progress and differences with respect to discrete versus spatially coincident (mixed) compositions, models, and validation.

Number of materials[a]	Spatial relationship	Measurement	Models	Validation	References
3 to 4	Discrete	Identification	Phantoms *Ex vivo* tissue	n/a	15–17
3 to 4	Discrete	Quantification	Phantoms *Ex vivo* tissue	MAE	18–24
3	Mixed	Quantification	Phantoms	MAE	15, 21, 24, 25
3 to 4	Mixed	Quantification	*In vivo*	None	24, 25
4	Mixed	Quantification	Phantoms	AUC, MAE, and RMSE	This study

Note: AUC, area under the receiver operating characteristic curve; MAE, mean absolute error; n/a, not applicable; RMSE, root-mean-squared error.
[a]The total number of materials includes water.

transformative potential for spectral CT in clinical diagnostic imaging.

Therefore, the objective of this study was to demonstrate and validate quantitative material decomposition of multiple mixed, or spatially coincident, contrast agent and tissue compositions using photon-counting spectral CT. Iodine and gadolinium were selected for investigation due to their use as contrast agents in clinical diagnostic imaging with CT and MRI, respectively; calcium was included to simulate mineralized tissue. Material decomposition was performed using constrained maximum likelihood estimation (MLE) in the image domain. The accuracy of material decomposition was systematically and quantitatively evaluated by the root-mean-squared error (RMSE), sensitivity, specificity, and area under the receiver operating characteristic curve (AUC) on material concentration maps of calcium, gadolinium, and iodine.

2 Materials and Methods

2.1 *Calibration Phantom of Pure Discrete Compositions*

Gadolinium (III) nitrate hexahydrate, $Gd(NO_3)_3 \cdot 6H_2O$ (Acros Organics, 99.9%), solutions were prepared in deionized (DI) water at 0, 50, and 100 mM (0, 7.8, and 15.7 mg/mL, respectively) concentration. Iohexol (TCI Chemicals, >98.0%) solutions were also prepared in DI water at 0, 50, and 100 mM (0, 6.3, and 12.6 mg/mL, respectively) concentration. Calcium chloride dihydrate, $CaCl_2 \cdot 2H_2O$ (Sigma-Aldrich, ≥99.9%), solutions were prepared in DI water at 0, 1450, and 2900 mM (0, 58, and 116 mg/mL, respectively) concentration, which were chosen to match the total attenuation of gadolinium nitrate across the overall photon energy spectrum of the polychromatic x-ray source (~20 to 80 keV). Calibration concentrations were chosen to significantly exceed estimated sample concentrations to achieve greater accuracy and less variability in image-based material decomposition by maximizing the signal-to-noise ratio for each component.[26] Eppendorf tubes (5 mm inner diameter) containing each discrete composition and concentration (7 in total) were placed in a modular acrylic phantom (35 mm outer diameter) for imaging in a single acquisition. A polytetrafluoroethyelene screw was present at the center of the phantom as part of a clamping mechanism for holding Eppendorf tubes within the phantom and was excluded from material decomposition.

2.2 *Sample Phantom of Mixed Compositions*

A sample phantom comprised mixed combinations of 0, 10, and 20 mM (0, 1.6, and 3.1 mg/mL, respectively) concentrations of gadolinium nitrate; 0, 10, and 20 mM (0, 1.3, and 2.5 mg/mL, respectively) concentrations of iohexol; and 0, 290 and 580 mM (0, 11.6, and 23.2 mg/mL, respectively) concentrations of calcium chloride (27 in total) in DI water. The range of contrast agent concentrations was selected to be feasible for *in vivo* targeted delivery to a site of interest, based upon previous preclinical animal models, while challenging the detection limit of conventional CT.[27] Calcium chloride concentrations were chosen to match the total attenuation of gadolinium nitrate across the overall photon energy spectrum and thus presented a challenge for material decomposition of a contrast agent coincident with mineralized tissue. Eppendorf tubes containing each mixed composition and concentration (27 in total) were placed in the same modular phantom for imaging in 6 acquisitions.

2.3 *Image Acquisition*

Calibration and sample phantoms were imaged using a commercially available spectral CT (MARS-12 v.5, MARS Bioimaging Ltd., Christchurch, New Zealand) equipped with a polychromatic x-ray source operating at 80 kVp, 1.96 mm aluminum beam filtration, and a photon-counting detector comprising a CdZnTe semiconductor sensor, 2 mm in thickness, bonded to a Medipix 3RX chip[12,28] with 110 μm pixels and 5 energy bins with charge summing mode. Images were acquired using a helical scan with 1440 projections per rotation. Images were acquired with an integration time of 100 ms resulting in an average of 1000 counts in each detector pixel. The excitation current was set to 16 μA to produce a photon count rate of 10 counts/ms in order to mitigate the effects of pulse pileup. Detector energy thresholds were set at 19, 29, 39, and 50 keV to leverage the *k*-edge discontinuities of iodine and gadolinium at 33.2 and 50.2 keV, respectively. An arbitration counter is also present at 7 keV, such that the 5 energy bins were 7 to 19, 19 to 29, 29 to 39, 39 to 50, and 50 to 80 keV. Reconstructions were performed with a 100 μm isometric voxel size and a nominal spatial resolution of ~300 μm. For representative images,

grayscale intensities were converted to Hounsfield units (HU) by calibration with air (−1000 HU) and water (0 HU).

2.4 *Material Decomposition*

Material decomposition of spatially coincident calcium (Ca), gadolinium (Gd), iodine (I), and water was performed using constrained MLE in the image domain, adapting methods previously demonstrated for spatially discrete compositions.[26] Detailed methods are provided in the Appendix. Briefly, MLE was calibrated by an $M \times N$ material basis matrix, where M is the number of energy bins and N is the number of materials to be decomposed. The material basis matrix was established by multiple linear least squares regression of the x-ray attenuation measured in each energy bin versus known concentrations of each material composition in the calibration phantom. The x-ray attenuation was measured as the mean attenuation within a 14.6 mm^3 cuboidal volume of interest (VOI) located at the center of each Eppendorf tube in the calibration phantom images. Elemental volume fractions were estimated from the known concentrations of compositions in the calibration phantom based upon the mass and density of the elemental component (Ca, Gd, or I) and water.

The volume fraction, or fractional abundance, of materials in each voxel of sample phantom images was determined by MLE using a quadratic programming function, *quadprog*, in MATLAB (v.9.0, Mathworks Inc.) such that solutions to the linear system of equations were constrained to full additivity and non-negativity.[29] The estimated elemental volume fractions of unknown sample compositions were then scaled to millimolar (mM) concentration using the material basis matrix and linear regression model determined from the calibration phantom.

The accuracy of material decomposition was evaluated from sample phantom images using a 7.9 mm^3 cuboidal VOI, including 45 slices of the reconstruction, located at the center of each Eppendorf tube. Sensitivity and specificity for detecting each component (Ca, Gd, or I) in true positive and true negative voxels, respectively, were measured at a 5 mM threshold. Mixtures containing 290 mM calcium, 10 mM gadolinium, and 10 mM iodine were selected as true positive VOIs (9 in total) for each component. An equal total number of true negative VOIs (9 in total) were selected as those containing 0 mM of the component of interest (Ca, Gd, or I) but identical concentrations to the true positive VOIs for the other components. AUC was calculated by evaluating sensitivity and specificity over a range of concentration thresholds (0 to 1000 mM or 0 to 40 mg/mL Ca, 0 to 30 mM or 0 to 4.7 mg/mL Gd, and 0 to 30 mM or 0 to 3.8 mg/mL I), which exceeded the concentrations within the sample phantom, to determine sets of positive and negative voxels. The quantitative accuracy of material decomposition was evaluated by the RMSE of all estimated versus known concentrations for each component (Ca, Gd, or I) pooled over mixed compositions (27 in total). The overall effects of each component (Ca, Gd, and I) in mixed compositions, and binary interactions (Ca × Gd, Ca × I, and I × Gd), on the concentrations estimated by material decomposition were examined using multiple regression (JMP® 13.0, SAS Institute Inc.).

3 Results

Grayscale images of pure compositions in the calibration phantom exhibited increased x-ray attenuation with an increased concentration of each composition, as expected [Fig. 1(a)]. The *k*-edge discontinuity of gadolinium and iodine was evident by deviations in the expected trend of decreased attenuation with increased photon energy at fixed concentration, or a sharp change in the linear slope of attenuation versus concentration. The measured x-ray attenuation in each photon energy bin versus known concentrations of each material composition (Ca, Gd, and I) in the calibration phantom (Fig. 1) exhibited a strong linear correlation ($R^2 > 0.91$, Table 2) with low error (RMSE < 1.8%). The strong correlation and low error of the multiple linear regression models were critical for enabling accurate material decomposition mixed compositions using MLE.

Material decomposition of each component (Ca, Gd, and I) in mixed compositions of the sample phantom provided color material concentration maps that clearly identified and differentiated each material (Fig. 2). In contrast, these materials were indistinguishable in representative CT images even as pure compositions [Fig. 1(a)], let alone mixed compositions [Fig. 2(a)]. Voxel-based classification metrics indicated that material decomposition of each component (Ca, Gd, and I) was highly accurate, exhibiting AUC > 0.95 and specificity > 0.92 (Table 3). The sensitivity of detecting calcium and iodine was 0.94, whereas gadolinium was lower at 0.70.

Material decomposition also provided accurate quantitative estimates of material concentrations in mixed compositions with RMSE <12% of the maximum concentration for each component (Table 3). Importantly, more than 95%, 97%, and 98% of variability in the estimated concentration of calcium, gadolinium, and iodine, respectively, were predicted by the primary

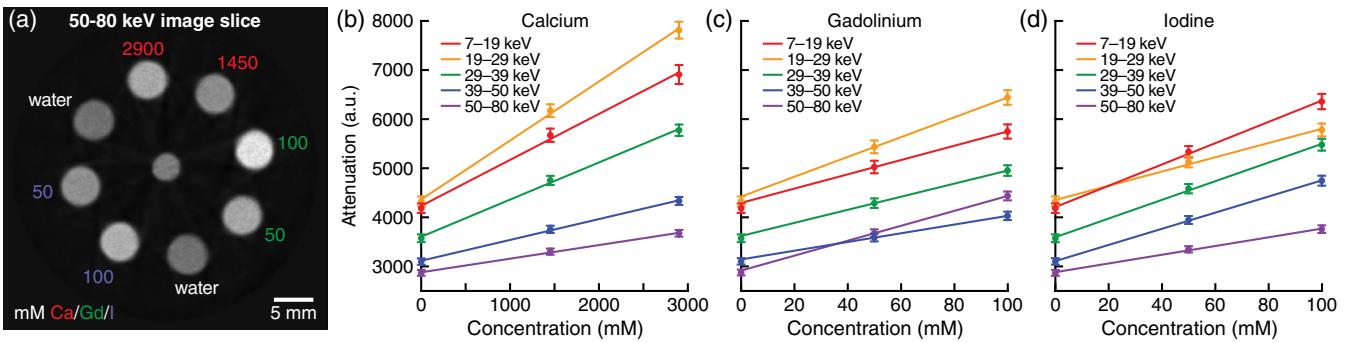

Fig. 1 (a) Representative grayscale CT image slice of the calibration phantom at the highest energy bin (50 to 80 keV). Linear regressions of the measured x-ray attenuation in each photon energy bin versus known concentrations of (b) gadolinium, (c) iodine, and (d) calcium in the calibration phantom. Regression coefficients are tabulated in Table 2.

Table 2 Linear least squares regression of the measured x-ray attenuation, y (a.u.), in each photon energy bin versus known concentrations, x (mM), of each material component (Ca, Gd, and I) in the calibration phantom. RMSE was calculated as a percent of the maximum signal.

	Individual regressions						Multiple regression model	
Energy bin	Ca	R^2	Gd	R^2	I	R^2	R^2	RMSE (%)
7 to 19 keV	$y = 0.9 \cdot x + 4233$	0.98	$y = 14.6 \cdot x + 4294$	0.88	$y = 21.7 \cdot x + 4209$	0.98	0.91	1.8
19 to 29 keV	$y = 1.2 \cdot x + 4364$	0.99	$y = 20.2 \cdot x + 4423$	0.93	$y = 14.5 \cdot x + 4352$	0.96	0.94	1.7
29 to 39 keV	$y = 0.8 \cdot x + 3603$	0.99	$y = 13.3 \cdot x + 3620$	0.92	$y = 19.0 \cdot x + 3595$	0.98	0.93	1.7
39 to 50 keV	$y = 0.4 \cdot x + 3115$	0.98	$y = 8.9 \cdot x + 3142$	0.89	$y = 16.4 \cdot x + 3109$	0.98	0.91	1.6
50 to 80 keV	$y = 0.3 \cdot x + 2880$	0.96	$y = 15.2 \cdot x + 2915$	0.96	$y = 8.9 \cdot x + 2882$	0.96	0.96	1.7

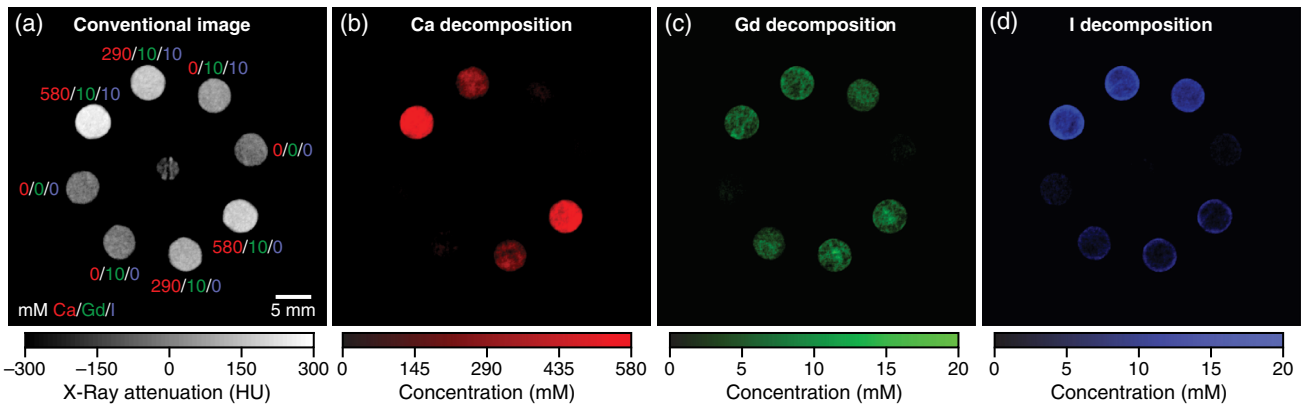

Fig. 2 Representative image slices of a sample phantom with mixed, or spatially coincident, compositions comprising calcium (Ca) at 0, 290, and 580 mM (0, 11.6, and 23.2 mg/mL, respectively) concentration; gadolinium (Gd) at 0 and 10 mM (0 and 1.6 mg/mL, respectively) concentration; and iodine (I) at 0 and 10 mM (0 and 1.3 mg/mL, respectively) concentration: (a) grayscale CT image slice at the highest energy bin (50 to 80 keV) and quantitative material decomposition maps for (b) Ca (red), (c) Gd (green), and (d) I (blue). Grayscale intensities were converted to HU and color intensities were scaled to mM concentrations.

Table 3 Overall spatial (sensitivity, specificity, and AUC) and quantitative (RMSE and average absolute error) accuracy of material decomposition for mixed compositions of calcium (Ca), gadolinium (Gd), and iodine (I) in water.

Metric	Ca	Gd	I
Sensitivity	0.94	0.70	0.94
Specificity	0.93	0.98	0.92
AUC	0.98	0.95	0.98
RMSE (mM)	58.5	2.39	1.45
RMSE (mg/mL)	2.34	0.38	0.18
RMSE (%)	10.1	11.9	7.3
Absolute error (mM)	22.2	−1.6	1.0
Absolute error (mg/mL)	0.89	−0.24	0.13
Absolute error (%)	3.9	−7.8	5.2

effect of each respective component alone by linear regression. Nonetheless, multiple linear regression models showed that estimated concentrations of calcium were influenced by the presence of either iodine or gadolinium, including an interaction between calcium and iodine (Table 4). Estimated concentrations of gadolinium were also influenced by iodine (Table 4).

4 Discussion

Photon-counting spectral CT enabled quantitative molecular imaging of multiple spatially coincident contrast agent (gadolinium and iodine) and tissue (calcium and water) compositions (Fig. 2) with high accuracy (AUC > 0.95, RMSE < 12%, Table 3). In fact, the AUC and RMSE for material decomposition of the mixed compositions were similar to that previously reported for material decomposition of a single discrete contrast agent using similar image acquisition and material decomposition methods.[26] Thus, the relatively minor errors that were observed were most likely due to artifacts and inherent noise in the acquired images that were propagated to the material decomposition in the image domain, and/or assumptions in the material decomposition methods, and were not noticeably

Table 4 The overall effects of each component in mixed compositions, and binary interactions, on the concentrations estimated by material decomposition. Italicized *p*-values show statistically significant effects from the multiple regression model. Note that the primary effect of respective each component (bold and italicize) in a single-factor model predicted more than 95%, 97%, and 98% of variability in the estimated concentration of calcium (Ca), gadolinium (Gd), and iodine (I), respectively; therefore, other statistically significant effects were relatively minor.

	Components in mixed compositions							
Estimated concentrations	Ca	Gd	I	Ca × Gd	Ca × I	I × Gd	RMSE (%)	R^2
Ca	***<0.0001***	*<0.01*	*<0.0001*	0.99	*<0.001*	0.14	3.9	0.99
Gd	0.76	***<0.0001***	*<0.05*	0.75	0.28	0.28	6.4	0.98
I	0.62	0.28	***<0.0001***	0.63	0.58	0.93	5.8	0.98

compounded by the decomposition of multiple spatially coincident compositions. However, further work is needed to investigate the relative contributions of these sources of error.

Images in this study were known to include two artifacts. A geometric misalignment, specifically a 1 mm offset of the source and detector, was discovered during the course of this study and was observed to produce a reconstruction artifact observed as relatively higher concentration around the periphery of sample phantom compositions, most noticeably in the iodine concentration map [Fig. 2(d)]. Additionally, a ring artifact was observed due to the presence of physical gaps between the three detector chips. These artifacts were small and not readily visible in images but certainly contributed to the observed error in image-based material decomposition. Therefore, the accuracy of the material decomposition results, in spite of these image artifacts, is encouraging and suggests that the image-based material decomposition was relatively robust against image artifacts.

To minimize the effects of inherent image noise on material decomposition, material concentrations in the calibration phantom were chosen to be much greater than those measured in the sample phantom, without starving the detector. Calibration concentrations that significantly exceed estimated sample concentrations were previously shown to result in greater accuracy and less variability in image-based material decomposition due to maximizing the signal-to-noise ratio for each component.[26] Therefore, calibration with lower concentrations, comparable in magnitude to those measured in the sample phantom, would be expected to result in greater error and variability than that observed in this study.

Assumptions required to constrain the solution space for material decomposition may also influence error in quantitative estimates.[30] In this study, the material decomposition was volume-constrained, and the overall volume fraction of each elemental component was allowed to increase with the addition of solute (e.g., Gd) to solvent (water).[26] Unfortunately, there is no constraint that perfectly describes the physical system. For example, calcium concentrations were sufficiently high to increase the overall volume of aqueous solutions, but the effects of gadolinium and iodine concentrations on the overall volume of aqueous solutions were negligible. Therefore, these differing effects for different components within mixed compositions could skew the results of quantitative material decomposition and warrant further investigation.

The relatively low sensitivity and high specificity for gadolinium compared with calcium and iodine were due to an underestimation of the gadolinium concentration (average error = −1.6 mM or −0.25 mg/mL, Table 3), which resulted in more voxels within the selected VOI falling below the 5 mM threshold used for the analysis of sensitivity and specificity. The voxel-based classification analysis in this study is expected to underestimate sensitivity, specificity, and AUC compared with object-based classification analysis. Comparison of voxel-based classification metrics between studies requires caution due to dependence on the voxel size and reconstruction methods. Nonetheless, the AUC for material decomposition of gadolinium and iodine within mixed compositions was similar to that previously reported for material decomposition of a single discrete contrast agent using a similar voxel-based classification analysis.[26] The RMSE for material decomposition of gadolinium and iodine within mixed compositions was also similar to that previously reported for each single component.[26,31] Therefore, the ability to decompose multiple mixed, or spatially coincident, compositions with comparable accuracy to pure discrete compositions is encouraging for potential preclinical and clinical applications.

Estimated concentrations of calcium were more susceptible to error caused by the influence of mixed compositions than was gadolinium or iodine (Table 4). Gadolinium and iodine exhibited a *k*-edge discontinuity within the observed photon energy spectrum but calcium did not. Materials that lack a *k*-edge discontinuity within the photon energy spectrum typically exhibit similar attenuation profiles with only subtle differences that are more difficult to resolve and thus pose a greater challenge to material decomposition. Likewise, minor errors in the estimated concentrations of calcium and gadolinium due to the presence of iodine in mixed compositions (Table 4) were mostly likely due to similarity in the attenuation profiles since the attenuation profile of iodine lies in between that of calcium and gadolinium. In both cases, the decomposition of calcium and iodine relied heavily on the measured attenuation at low photon energies.

The decomposition of multiple, spatially coincident materials lacking a *k*-edge discontinuity or with similar attenuation profiles, which may depend heavily on low photon energy bins, may be more challenging in clinical imaging of human subjects than in this study. The feasibility of clinical translation will depend on the type of image acquisition (e.g., CT versus mammography), reconstruction methods, and detector performance. In this study, the maximum number of photon energy bins (5) and minimum photon energy bin bandwidth (10 keV) were limited by the number of charge summing thresholds and spectral resolution, respectively, of the photon-counting detector. Continued progress in photon-counting detector technology is anticipated to enable increased photon counts and higher spectral resolution (e.g., Timepix),[32] which will further improve

the accuracy of material decomposition, especially for materials lacking a k-edge discontinuity, and accelerate clinical translation.

Photon-counting spectral CT enabled the decomposition and quantification of low concentrations of gadolinium and iodine that were spatially coincident with high concentrations of calcium. This result suggests that spectral CT may be used to decompose and quantify low concentrations of contrast agents that are spatially coincident with mineralized tissues,[33] such as breast microcalcifications,[34,35] atherosclerotic plaque,[15] and bone.[36,37] The ability to decompose and quantify spatially coincident gadolinium and iodine further suggests that spectral CT may be used for multicontrast imaging,[23–25,38] including perfusion, angiography, colonography, and/or tumor targeting.

5 Conclusions

Individual material components (Ca, Gd, and I) within mixed, or spatially coincident, compositions were identified and quantified with high accuracy (AUC > 0.95, RMSE < 12%) using photon-counting spectral CT and material decomposition by MLE in the image domain. Thus, photon-counting spectral CT enabled quantitative molecular imaging of multiple spatially coincident contrast agent (gadolinium and iodine) and tissue (calcium and water) compositions, which is not possible with current clinical molecular imaging modalities, such as nuclear imaging and MRI.

6 Appendix: Detailed Methods for Material Decomposition

MLE was calibrated by a material basis matrix, C, an $M \times N$ matrix of attenuation coefficients for each discrete material in each energy bin, where M is the number of energy bins and N is the number of materials to be decomposed. Attenuation is assumed to be approximately linear for each material in each photon energy bin. The measured effective attenuation within the j-th voxel for the k-th energy bin is described by

$$\bar{\mu}_{jk} = \sum_{i=1}^{N} (\mu_{ijk} \cdot x_i), \tag{1}$$

where N is the total number of materials to be identified, μ_i is the mass attenuation coefficient of the i-th material, and x_i is the volume fraction (or fractional abundance) of the i-th material. The estimated attenuation coefficient of each discrete material (Ca, Gd, and I) in the k-th energy bin was determined for the material basis matrix by multiple least squares linear regression with known material concentrations as

$$\bar{\mu}_k = b_o + b_i x_i + b_{\text{water}} x_{\text{water}}, \tag{2}$$

where $\bar{\mu}_k$ is the effective attenuation of voxels within the measured VOI, b_o is the intercept, which was assumed to be zero, b_i is the estimated attenuation of the i-th material, and b_{water} is the estimated attenuation of water. Elemental volume fractions were estimated from known concentrations of materials in the calibration phantom as

$$v_i \approx \frac{(m_i/\rho_i)}{(m_i/\rho_i) + (m_{\text{water}}/\rho_{\text{water}})}, \tag{3}$$

where v_i is the estimated volume fraction of the i-th material (Ca, Gd, or I), m_i and m_{water} are the masses of the i-th material and water, respectively, and ρ_i and ρ_{water} are the densities of the i-th material and water, respectively, which were assumed to be constant, such that $v_{\text{water}} \approx 1 - v_i$. The densities of calcium, gadolinium, iodine, and water were taken as 1.54, 7.90, 4.93, 1.00 g/cm^3, respectively. The multivariate linear model of Eq. (2) was then used to solve for the attenuation coefficients by substituting the fractional abundance, x_i, with the elemental volume fraction of each material, v_i, and $\bar{\mu}_k$ with the mean x-ray attenuation of each material and concentration measured within a 14.6 mm^3 cuboidal VOI in the calibration phantom. The multivariate model was repeated for each of the five energy bins to complete the basis matrix (C).

Material decomposition of unknown concentrations of calcium, gadolinium, iodine, and water sample phantom images was performed by MLE using a quadratic programming function, *quadprog*, in MATLAB (v.9.0, Mathworks Inc.) and the material basis matrix. Constrained MLE was chosen to mitigate the large number of possible solutions to the linear system of equations, which were constrained to satisfy both full additivity and non-negativity. The volume fraction of materials in each voxel of sample phantom images was estimated by minimizing the following equation:

$$\min_x 0.5 \cdot x^T \cdot H \cdot x + f^T \cdot x, \tag{4}$$

where x is a vector of volume fractions of length N, and

$$H = 2 \cdot C^T \cdot C, \tag{5}$$

$$f = -2 \cdot C^T \cdot \mu_M, \tag{6}$$

where μ_M is a vector of length M containing the attenuation values of the unknown sample in each energy bin, constrained such that,

$$A \cdot x \leq b, \tag{7}$$

$$A_{\text{eq}} \cdot x = b_{\text{eq}}, \tag{8}$$

$$A = \begin{bmatrix} 1 & 0 & 0 \\ 0 & \ddots & 0 \\ 0 & 0 & 1_N \\ -1 & 0 & 0 \\ 0 & \ddots & 0 \\ 0 & 0 & -1_N \end{bmatrix}, \tag{9}$$

where b is an $N \times 2$ vector containing N ones and N zeros, A_{eq} is a vector of length N comprised ones, and b_{eq} is equal to one. Equation (7) limits the solution to remain between 0 and 1, satisfying the non-negativity constraint. Equation (8) ensures that the vector of volume fractions sums to 1 for each voxel, satisfying the full additivity constraint. Volume fractions were calculated for material in each unknown sample.

After material decomposition, the estimated material volume fractions in unknown sample compositions were scaled to mM concentration. The mean x-ray attenuation was determined for known concentrations of each material composition in the calibration phantom for each energy bin. The mean attenuation values were then decomposed using constrained MLE for each of material in the basis matrix. Estimated volume fractions were correlated with the known concentrations (mM) in the calibration phantom for each material composition using linear least

squares regression. The intercept, b_o, was allowed to be nonzero. Decomposed images were then scaled to mM concentrations using this linear regression model to create concentration maps for each material.

Disclosures

No conflicts of interest, financial or otherwise, are declared by the authors.

Acknowledgments

This research was supported by grants from the National Science Foundation (DMR-1309587), the Kelly Cares Foundation, St. Joseph Health System, and the University of Notre Dame Equipment Renewal and Restoration Program. T.E.C. was supported by the Martell Family PhD Fellowship at the University of Notre Dame. The authors acknowledge the Notre Dame Center for Environmental Science and Technology (CEST) for ICP-OES and the Notre Dame Integrated Imaging Facility (NDIIF).

References

1. W. A. Kalender, "X-ray computed tomography," *Phys. Med. Biol.* **51**(13), R29–R43 (2006).
2. M. F. Kircher and J. K. Willmann, "Molecular body imaging: MR imaging, CT, and US. Part I. Principles," *Radiology* **263**, 633–643 (2012).
3. S. Y. Nam et al., "Imaging strategies for tissue engineering applications," *Tissue Eng. Part B Rev.* **21**, 88–102 (2015).
4. A. R. Kherlopian et al., "A review of imaging techniques for systems biology," *BMC Syst. Biol.* **2**, 74 (2008).
5. C. J. Anderson et al., "^{64}Cu-TETA-octreotide as a PET imaging agent for patients with neuroendocrine tumors," *J. Nucl. Med.* **42**, 213–221 (2001).
6. M. Beheshti et al., "Detection of bone metastases in patients with prostate cancer by ^{18}F fluorocholine and ^{18}F fluoride PET-CT: a comparative study," *Eur. J. Nucl. Med. Mol. Imaging* **35**, 1766–1774 (2008).
7. R. E. Alvarez and A. Macovski, "Energy-selective reconstructions in x-ray computerized tomography," *Phys. Med. Biol.* **21**(5), 733–744 (1976).
8. T. R. Johnson et al., "Material differentiation by dual energy CT: initial experience," *Eur. Radiol.* **17**, 1510–1517 (2007).
9. A. Primak et al., "Improved dual-energy material discrimination for dual-source CT by means of additional spectral filtration," *Med. Phys.* **36**, 1359–1369 (2009).
10. P. R. S. Mendonça, P. Lamb, and D. V. Sahani, "A flexible method for multi-material decomposition of dual-energy CT images," *IEEE Trans. Med. Imaging* **33**, 99–116 (2014).
11. L. Yu et al., "Dual-source multienergy CT with triple or quadruple x-ray beams," *J. Med. Imaging* **5**, 033502 (2018).
12. R. Ballabriga et al., "Medipix3: a 64 k pixel detector readout chip working in single photon counting mode with improved spectrometric performance," *Nucl. Instrum. Methods. Phys. Res. A* **633**, S15–S18 (2011).
13. P. Delpierre, "A history of hybrid pixel detectors, from high energy physics to medical imaging," *J. Instrum.* **9**, C05059 (2014).
14. K. Taguchi, "Energy-sensitive photon counting detector-based x-ray computed tomography," *Radiol. Phys. Technol.* **10**, 8–22 (2017).
15. D. P. Cormode et al., "Atherosclerotic plaque composition: analysis with multicolor CT and targeted gold nanoparticles," *Radiology* **256**, 774–782 (2010).
16. N. G. Anderson et al., "Spectroscopic (multi-energy) CT distinguishes iodine and barium contrast material in mice," *Eur. Radiol.* **20**, 2126–2134 (2010).
17. M. F. Walsh et al., "Spectral CT data acquisition with Medipix3.1," *J. Instrum.* **8**, P10012 (2013).
18. J.-P. Schlomka et al., "Experimental feasibility of multi-energy photon-counting K-edge imaging in pre-clinical computed tomography," *Phys. Med. Biol.* **53**(15), 4031–4047 (2008).
19. D. Pan et al., "Computed tomography in color: NanoK-enhanced spectral CT molecular imaging," *Angew. Chem. Int. Ed.* **49**, 9635–9639 (2010).
20. A. M. Alessio and L. R. MacDonald, "Quantitative material characterization from multi-energy photon counting CT," *Med. Phys.* **40**, 031108 (2013).
21. M. Perrson et al., "Energy-resolved CT imaging with a photon-counting silicon-strip detector," *Phys. Med. Biol.* **59**, 6709–6727 (2014).
22. T. L. McGinnity et al., "Hafnia (HfO_2) nanoparticles as an x-ray contrast agent and mid-infrared biosensor," *Nanoscale* **8**, 13627–13637 (2016).
23. D. Muenzel et al., "Spectral photon-counting CT: initial experience with dual-contrast agent K-edge colonography," *Radiology* **283**, 723–728 (2017).
24. D. P. Cormode et al., "Multicolor spectral photon-counting computed tomography: in vivo dual contrast imaging with a high count rate scanner," *Sci. Rep.* **7**, 4784 (2017).
25. R. Symons et al., "Photon-counting CT for simultaneous imaging of multiple contrast agents in the abdomen: an in vivo study," *Med. Phys.* **44**(10), 5120–5127 (2017).
26. T. E. Curtis and R. K. Roeder, "Effects of calibration methods on quantitative material decomposition in photon-counting spectral computed tomography using a maximum a posteriori estimator," *Med. Phys.* **44**(10), 5187–5197 (2017).
27. L. E. Cole et al., "Gold nanoparticles as contrast agents in x-ray imaging and computed tomography," *Nanomedicine* **10**(2), 321–341 (2015).
28. E. N. Gimenez et al., "Characterization of Medipix3 with synchrotron radiation," *IEEE Trans. Nucl. Sci.* **58**(1), 323–332 (2011).
29. K. Themelis and A. A. Rontogiannis, "A soft constrained MAP estimator for supervised hyperspectral signal unmixing," in *16th Eur. Signal Process. Conf.* (2008).
30. X. Liu et al., "Quantitative imaging of element composition and mass fraction using dual-energy CT: three-material decomposition," *Med. Phys.* **36**(5):1602–1609 (2009).
31. S. Si-Mohamed et al., "Evaluation of spectral photon counting computed tomography K-edge imaging for determination of gold nanoparticle biodistribution in vivo," *Nanoscale* **9**, 18246–18257 (2017).
32. B. Zat'ko et al., "Imaging performance of a Timepix detector based on semi-insulating GaAs," *J. Instrum.* **13**, C01034 (2018).
33. L. E. Cole, T. Vargo-Gogola, and R. K. Roeder, "Targeted delivery to bone and mineral deposits using bisphosphonate ligands," *Adv. Drug Delivery Rev.* **99**, 12–27 (2016).
34. L. E. Cole, T. Vargo-Gogola, and R. K. Roeder, "Contrast-enhanced x-ray detection of breast microcalcifications in a murine model using targeted gold nanoparticles," *ACS Nano* **8**(7), 7486–7496 (2014).
35. L. E. Cole, T. Vargo-Gogola, and R. K. Roeder, "Contrast-enhanced x-ray detection of microcalcifications in radiographically dense mammary tissue using targeted gold nanoparticles," *ACS Nano* **9**(9), 8923–8932 (2015).
36. M. D. Landrigan et al., "Contrast-enhanced micro-computed tomography of fatigue microdamage accumulation in human cortical bone," *Bone* **48**(3), 443–450 (2011).
37. T. L. Turnbull et al., "Detection of fatigue microdamage in whole rat femora using contrast-enhanced micro-CT," *J. Biomech.* **44**(13), 2395–2400 (2011).
38. R. K. Roeder et al., "Nanoparticle imaging probes for molecular imaging with computed tomography and application to cancer imaging," *Proc. SPIE* **10132**, 101320X (2017).

Tyler E. Curtis received his BS degree in bioengineering from Michigan Technological University in 2014. Currently, he is a PhD candidate in the Bioengineering Graduate Program at the University of Notre Dame. His current research is focused on biomedical applications of photon-counting spectral computed tomography, including quantitative imaging of imaging probes and multimaterial decomposition.

Ryan K. Roeder received his PhD in materials engineering from Purdue University in 1999. He is a professor in the Bioengineering Graduate Program at the University of Notre Dame. His research interests cut across biomaterials, including nanoparticle imaging probes and tissue engineering scaffolds; biomechanics, including musculoskeletal tissues; and biomedical imaging, including contrast-enhanced CT and photon-counting spectral CT. His research interests have been supported by numerous federal agencies (e.g., NIH, NSF, etc.), industrial sponsors, and private foundations.